13. Cai, W. *et al.* in *Proc. 1st Annu. Int. Conf. on Computational Molecular Biology (RECOMB97)* 67–74 (Association for Computing Machinery, New York, 1997).
14. Smith, L. M. Automated synthesis and sequence analysis of biological macromolecules. *Anal. Chem.* **60,** 381A–390A (1988).
15. Fodor, S. P. A. *et al.* Light-directed, spatially addressable parallel chemical synthesis. *Science* **251,** 767–773 (1991).
16. Chee, M. *et al.* Accessing genetic information with high-density DNA arrays. *Science* **274,** 610–614 (1996).
17. Morimoto , N., Arita, M. & Suyama, A. in *Proc. DIMACS: DNA Based Computers (III)* (eds Rubin, H. & Wood, D. H.) 83–92 (American Mathematical Society, Providence, 1997).
18. Yoshida, H. & Suyama, A. in *Preliminary Proc. DIMACS: DNA Based Computers (V)* 9–20 (American Mathematical Society, Providence, 1999).
19. Schöning, U. in *Proc. 40th Annu. IEEE Conf. of Foundations of Computer Science (FOCS)* 410–414 (IEEE Computer Society, Los Alamitos, California, 1999).
20. Guo, Z., Guilfoyle, R. A., Thiel, A. J., Wang, R. & Smith, L. M. Direct fluorescence analysis of genetic polymorphisms by hybridization with oligonucleotide arrays on glass supports. *Nucl. Acid. Res.* **22,** 5456–5465 (1994).
21. Jordan, C. E., Frutos, A. G., Thiel, A. J. & Corn, R. M. Surface plasmon resonance imaging measurements of DNA hybridization adsorption and streptavidin/DNA multilayer formation at chemically modified gold surfaces. *Anal. Chem.* **69,** 4939–4947 (1997).
22. Bain, C. D. *et al.* Formation of monolayer films by the spontaneous assembly of organic thiols from solution onto gold. *J. Am. Chem. Soc.* **111,** 321–335 (1989).
23. Baskaran, N. *et al.* Uniform amplification of a mixture of deoxyribonucleic acids with varying GC content. *Genome Res.* **6,** 633–638 (1996).
24. Rees, W. A., Yager, T. D., Korte, J. & von Hippel, P. H. Betaine can eliminate the base pair composition dependence of DNA melting. *Biochemistry* **32,** 137–144 (1993).
25. Voss, K. O., Pieter Roos, K., Nonay, R. L. & Dovichi, N. J. Combating PCR bias in bisulfate-based cytosine methylation analysis. Betaine-modified cytosine deamination PCR. *Anal. Chem.* **70,** 3818–3823 (1998).
26. Farrell, R. E. DNA amplification. *Immunol. Invest.* **26,** 3–7 (1997).
27. Lyamichev, V. *et al.* Polymorphism identification and quantitative detection of genomic DNA by invasive cleavage of oligonucleotide probes. *Nature Biotechnol.* **17,** 292–296 (1999).
28. Pippenger, N. Developments in the synthesis of reliable organisms from unreliable components. *Proc. Symp. Pure Math.* **50,** 311–324 (1990).
29. Boneh, D., Dunworth, C., Lipton, R. J. & Sgall, J. DNA Based Computers II (eds Landweber, L. F. & Baum, E. B.) 163–170 (DIMACS Series in Discrete Mathematics and Theoretical Computer Science, Vol. 44, American Mathematical Society, Providence, 1999).
30. Karp, R. M., Kenyon, C. & Waarts, O. Error-resilient DNA computation. *Random Struct. Algor.* **15,** 450–466 (1999).
31. Gillmor, S. D., Thiel, A. J., Smith, L. M. & Lagally, M. G. Hydrophilic/hydrophobic patterned surfaces as templates for DNA arrays. *Langmuir* (submitted).
32. Gallop, M. A., Barrett, R. W., Dower, W. J., Fodor, S. P. A. & Gordon, E. M. Applications of combinatorial technologies to drug discovery. 1. Background and peptide combinatorial libraries. *J. Med. Chem.* **37,** 1233–1251 (1994).
33. Gordon, E. M., Barrett, R. W., Dower, W. J., Fodor, S. P. A. & Gallop, M. A. Applications of combinatorial technologies to drug discovery. 2. Combinatorial organic synthesis, library screening strategies, and future directions. *J. Med. Chem.* **37,** 1385–1401 (1994).

**Acknowledgements**

We thank S. Gillmor and J. Brockman for help with the preparation of the photopatterned read-out arrays, and M. Lagally for discussions. This work was supported by the Defense Advanced Research Projects Agency (DARPA) and the National Science Foundation.

Correspondence and requests for materials should be addressed to L.M.S. (e-mail: smith@chem.wisc.edu)

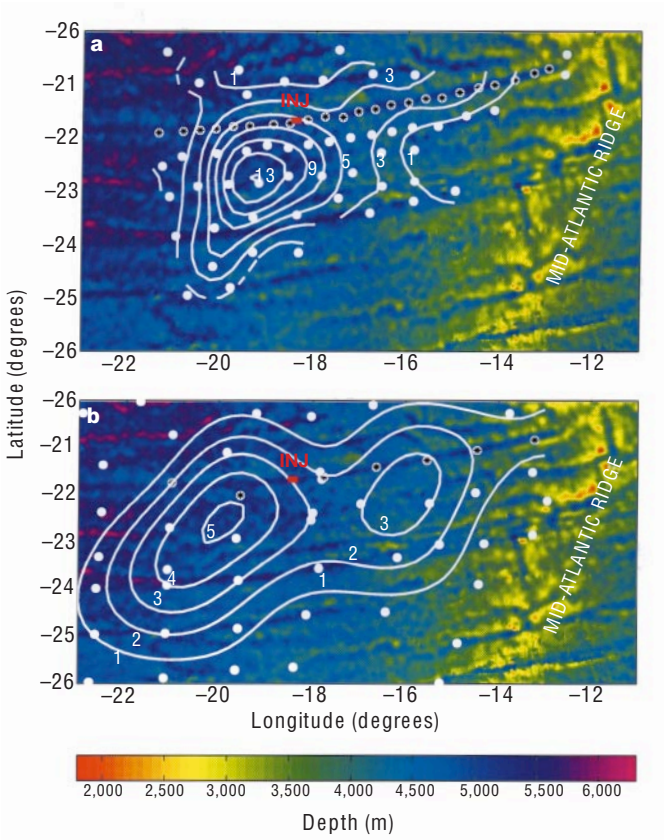


**Figure 1** Tracer distribution. **a**, 14 months after release; **b**, 26 months after release. The red bars labelled 'INJ' mark the release site of the tracer. The contours denote the column integral of $SF_6$ (in nmol $m^{-2}$) and colours denote bottom depth. The tracer mapping procedure did not take the bathymetry into account, and hence the meridional distribution in the east in **a** appears broader than the valleys where the stations are located and which actually hold most of the tracer. The bathymetry is from Smith and Sandwell[16]. The stations are shown as white dots; those with stars are used for the sections in Fig. 2. Southerly latitude and westerly longitude are shown negative.

# Evidence for enhanced mixing over rough topography in the abyssal ocean

**J. R. Ledwell, E. T. Montgomery, K. L. Polzin, L. C. St. Laurent, R. W. Schmitt & J. M. Toole**

*Woods Hole Oceanographic Institution, Woods Hole, Massachusetts 02543, USA*

**The overturning circulation of the ocean plays an important role in modulating the Earth's climate. But whereas the mechanisms for the vertical transport of water into the deep ocean—deep water formation at high latitudes—and horizontal transport in ocean currents have been largely identified, it is not clear how the compensating vertical transport of water from the depths to the surface is accomplished. Turbulent mixing across surfaces of constant density is the only viable mechanism for reducing the density of the water and enabling it to rise. However, measurements of the internal wave field, the main source of energy for mixing, and of turbulent dissipation rates, have typically implied diffusivities across surfaces of equal density of only ~0.1 $cm^2 s^{-1}$, too small to account for the return flow. Here we report measurements of tracer dispersion and turbulent energy dissipation in the Brazil basin that reveal diffusivities of 2–4 $cm^2 s^{-1}$ at a depth of 500 m above abyssal hills on the flank of the Mid-Atlantic Ridge, and approximately 10 $cm^2 s^{-1}$ nearer the bottom. This amount of mixing, probably driven by breaking internal waves that are generated by tidal currents flowing over the rough bathymetry, may be large enough to close the buoyancy budget for the Brazil basin and suggests a mechanism for closing the global overturning circulation.**

Our study was conducted in the abyssal Brazil basin where deep upwelling can be inferred from measurements of net inflow of dense water[4,5]. In 1996 we surveyed turbulent microstructure and internal wave fine-structure across the basin, and released 110 kg of sulphur hexafluoride above one of the zonal valleys on the western flank of the Mid-Atlantic Ridge[6] (Fig. 1). The microstructure data showed diapycnal mixing to be very low over the smooth parts of the Brazil

basin in the west, but greatly enhanced throughout much of the water column in the eastern part of the basin, with a distinct increase toward the bottom. The initial dispersion of the tracer during the first two weeks, and the microstructure measurements in its immediate vicinity, indicated diffusivities of about 0.5 $cm^2 s^{-1}$ at the isopycnal surface of the tracer release (45.9408 $kg m^{-3}$, referenced to 4,000 dbar). This surface was about 4,000 m deep, approximately 1,000 m above the valley floor and 500 m above the hilltops lying 20–30 km to the north and south of the release site. The microstructure data suggested still larger mixing rates to the east and closer to the bottom[6].

A second survey of the tracer and microstructure in 1997, 14 months after the release of the tracer, found about 95% of the tracer in a patch centred southwest of the release site (Fig. 1a). The remaining 5% was located as far as 500 km east of the release site, deep in the valley below the release, and as far as 300 km east in another zonal valley lying 200 km to the south. Tracer to the west peaked near the target density surface, while tracer to the east in the valleys was concentrated nearer the bottom (Fig. 2a). A third tracer survey in 1998, 26 months after its release, found about 70% of the tracer in the patch to the west, which had spread laterally and vertically, while the patch in the east had grown to include about 30% of the tracer and had dispersed dramatically across isopycnals (Figs 1b and 2b).

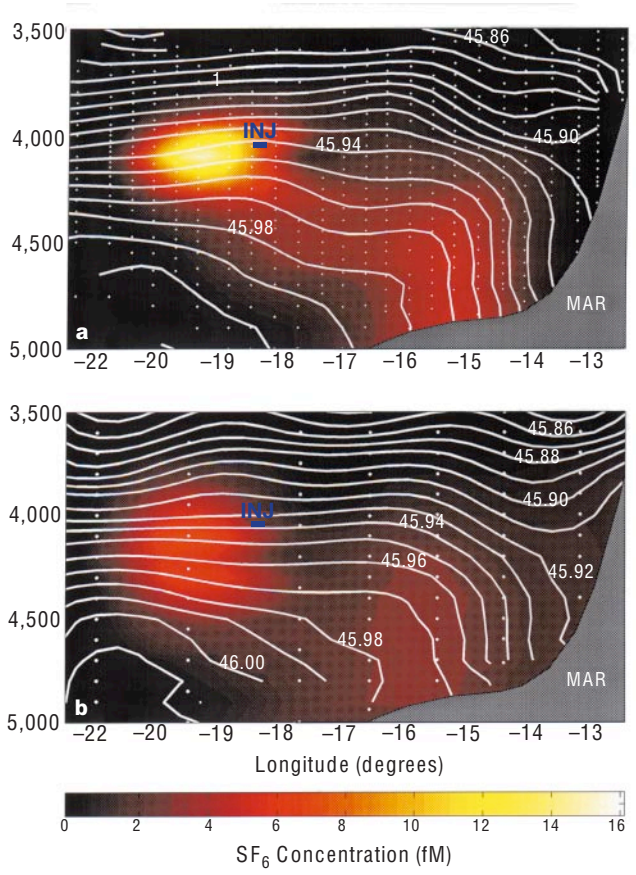


**Figure 2** Sections of tracer concentration and potential density from the valley where the tracer was released. **a**, 14 months after release; **b**, 26 months after release. The dots show the tracer sample locations, and the blue bar labelled 'INJ' marks the release site of the tracer. The sea floor (labelled MAR for Mid-Atlantic Ridge) is a polynomial fit to the soundings from the 14-month survey. The valley is enclosed by ridges to the north and south whose depths are indicated roughly where the white density contours (in $kg m^{-3}$) bend sharply down. The colours show the trace concentration: 1 fM = $10^{-15}$ M.

The inventory of tracer as a function of potential density has been estimated from all of the 1997 data and transformed into a profile of concentration versus height $z$ above the target density surface using the mean density profile west of 18° W (Fig. 3). The diapycnal diffusivity $K(z)$ was estimated by applying a one-dimensional model for the tracer evolution from the initial profile in 1996 to this 1997 profile (see Methods). Least-squares fits, shown in Fig. 3, were obtained for $K = 3.0\ cm^2 s^{-1}$ at $z = 0$ (~4,000 m depth), increasing to 8 $cm^2 s^{-1}$ at $z = -500$ m (~4,500 m depth). To obtain this fit it was necessary to include a velocity of the tracer relative to the water of $-1.0 \times 10^{-4}\ cm s^{-1}$. We can only suggest that tracer was transported on sinking particles, although the rate is at least a factor of 10 greater than that at a depth of 300 m in the subtropical North Atlantic[7]. It remains to be tested whether particulate effects are enhanced at high pressure and low temperature. This sinking continued at approximately the same rate between 1997 and 1998.

The three-dimensional tracer distributions of Figs 1 and 2 strongly suggest that diapycnal mixing on isopycnals increases toward the east as density surfaces approach the bottom. The one-dimensional model cannot account for this spatial variation, and so inferences from it are only approximate. In particular, because tracer found in the east is concentrated near the bottom, enhanced diffusion there tends to mix tracer from denser isopycnals back toward the target density surface; the model may thus underestimate the diffusivity on the deeper isopycnal surfaces. The estimate of $K$ at the target density surface seems to be accurate to within $\pm 1\ cm^2 s^{-1}$, although the depth dependence of $K$ is not well constrained with a one-dimensional model. Because only 5% of the tracer was in the east in 1997, the one-dimensional model seems justified. In 1998, 30% of the tracer was in the east and the transport back to lighter isopycnals seemed so pronounced that the one-dimensional approach has not been taken.

The diffusivity inferred from measurements of the dissipation of turbulent kinetic energy about the target surface in the region of the tracer patch was $2.3 \pm 1\ cm^2 s^{-1}$, similar to the tracer-derived value when adjustments for spatial and temporal biases in the sampling are taken into account (see Methods). Microstructure profiles clearly show an increase of diffusivity with decreasing height above the bottom (Fig. 4). A spatial bias toward low average diffusivity resulted from the location of most of the stations over valleys where the target isopycnal lay about 1,000 m above the local

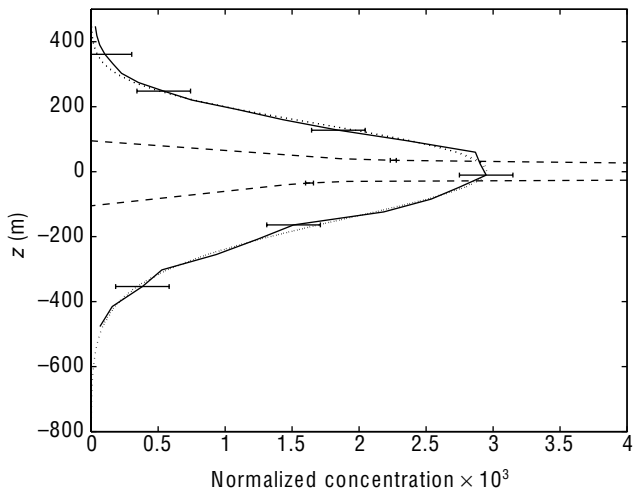


**Figure 3** Mean vertical tracer profiles (with uncertainties) and model fit. The dashed lines depict the initial condition. The solid line gives the 1997 tracer inventory in density space, transformed into height $z$ above the target density surface through the mean density profile west of 18° W. The dotted line is the least-squares fit to the solid line from the one-dimensional model.

bottom. Depth-averaged dissipation data from the 1997 survey document a fortnightly modulation in the mixing that lags the intensity of the barotropic tide by a few days (Fig. 5). Microstructure sampling in the vicinity of the main tracer patch occurred chiefly during minima in the fortnightly tidal cycle; this bias resulted in lower dissipation estimates there. Data from both the 1996 and 1997 cruises are biased in these ways, and consequently an earlier basin-average diffusivity estimate[6] is likely to be an underestimate.

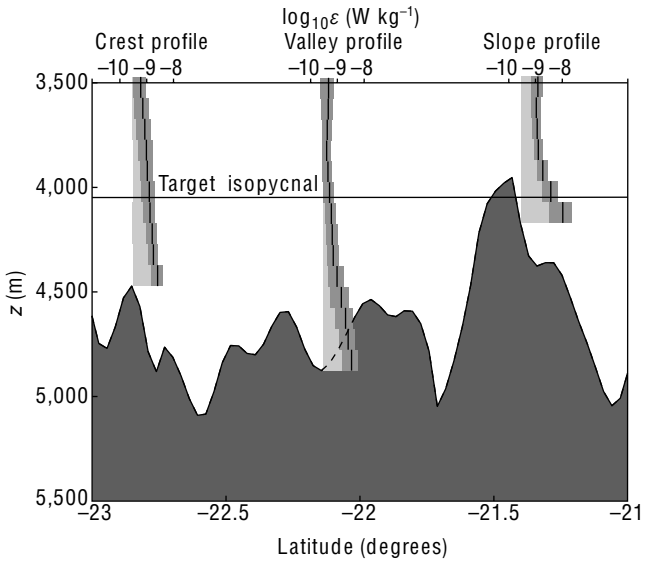


**Figure 4** Model profiles of turbulent kinetic energy dissipation rate. Profiles for crests, slopes, and valleys are shown along a section of meridional bathymetry at 18.5° W, the longitude of the tracer injection. The dark grey bands in the profiles indicate 95% confidence intervals about the mean estimates, shown as vertical line segments. The left edge of the light grey band is at $3 \times 10^{-10}$ W kg$^{-1}$ for reference. The average dissipation at the injection isopycnal, located at the horizontal line, is smaller over valleys than over crests and slopes.

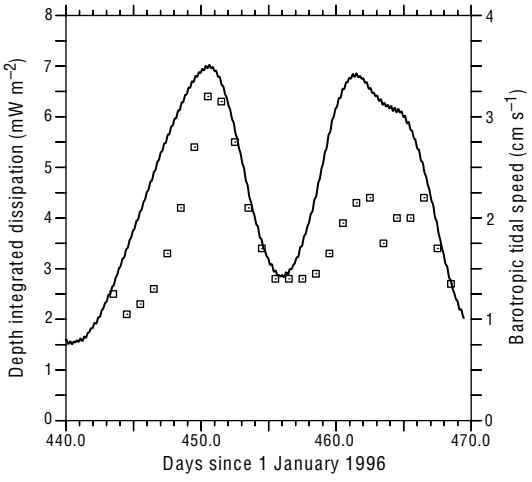


**Figure 5** Comparison of the turbulent energy dissipation rate and tidal speeds. The depth-integrated dissipation (squares) and model barotropic tidal speed (solid line: $(u^2 + v^2)^{1/2}$) are shown versus time for the 1997 cruise. A running three-day boxcar filter has been applied to both variables. The tidal velocity estimates[15] were extracted for the times and locations of the stations where the dissipation measurements were made.

The fortnightly cycle in the mixing (Fig. 5) supports the suggestion[6] that the enhanced mixing in the area results from the breaking of internal waves generated as the barotropic tide flows over the rough ridge bathymetry. Tidal flows over rough bathymetry efficiently generate upward-propagating internal waves with horizontal wavelengths ($\lambda$) characteristic of the bottom topography ($\lambda \lesssim 6$–$10$ km; ref. 8). Such waves can develop high shear at levels well above the bottom, and this shear can feed turbulent mixing[9]. The fortnightly modulation and small phase lag imply a spatially local balance between internal wave generation by tides and dissipation; the small time lag is consistent with the rate at which bottom-generated internal waves with vertical wavelengths of the order of 100 m can carry energy up into the water column where the waves interact with each other and break.

Both the one-dimensional tracer dispersion model and the dissipation measurements indicate that the diapycnal diffusivity increases sufficiently strongly with depth to imply a divergence of buoyancy flux and therefore that the diapycnal flow must be downward to maintain the density field. For example, the one-dimensional model indicates velocities of $-3 \times 10^{-5}$ to $-5 \times 10^{-5}$ cm s$^{-1}$ across isopycnals lying between the ridge tops and the target surface. Close to the bottom, however, there must be a convergence of turbulent buoyancy flux, as, except for a small geothermal flux[10], buoyancy and mass fluxes normal to the bottom must vanish. Hence, there must be a bottom layer in which the diapycnal component of the mean flow is toward decreasing density. This diapycnal flow could be a component of an eastward flow along the bottom. Indeed, a persistent eastward flow below the target density surface is indicated by the tracer plumes, although how much of this flow is along the bottom versus along isopycnals is a subject for further study.

Observations of cold bottom water flowing into the Brazil basin from the south imply upwelling across warmer isotherms and mixing supporting a basin-averaged diffusivity[4,5] of 2 to 4 cm$^2$ s$^{-1}$. Based on early results of our experiment extrapolated by bathymetric type to the whole basin, Polzin *et al.*[6] estimated a heat flux equivalent to an area-averaged diffusivity between 0.5 and 1.5 cm$^2$ s$^{-1}$ (dictated chiefly by the large dissipation values above the rough Mid-Atlantic Ridge). As the turbulent diffusivities reported here are a factor of two to three larger than those derived from the preliminary observations above the Mid-Atlantic Ridge, a revised estimate now closes the abyssal Brazil basin heat budget within the uncertainties. Moreover, our tracer and turbulence measurements provide guidance on extrapolating to the global ocean overturning problem, in particular by focusing attention on the role of barotropic tides and rough bathymetry in providing energy for mixing through the internal wave field. □

## Methods

### Tracer data

The average tracer concentration $C(z,t)$ on an isopycnal surface whose mean height is $z$, was modelled[11] by the equation:

$$A\frac{\partial C}{\partial t} + \frac{\partial}{\partial z}[A(w+W)C] = \frac{\partial}{\partial z}\left[AK\left(\frac{\partial C}{\partial z}\right)\right]$$

Here $A(z)$ is the area of the surface at height $z$ within a region encompassing all of the tracer, $w(z)$ is the vertical velocity of the water, and $W$ is an assumed constant vertical velocity of the tracer relative to the water. If the turbulent diffusivities for heat, salt, and tracer are the same, and the equation of state is approximated as linear, then the one-dimensional density equation gives:

$$\left(\frac{\partial z}{\partial t}\right)_\rho + w = \frac{\partial K}{\partial z} + \left(\frac{K}{A}\right)\frac{\partial A}{\partial z} + \left(\frac{K}{N^2}\right)\left(\frac{\partial N^2}{\partial z}\right)$$

Here $N$ is the buoyancy frequency. The first term represents temporal variation of isopycnal depths. Our observations in 1997 and 1998 indicate that this term is small relative to $w$, justifying its neglect below.

The depth dependence for $K(z)$, chosen with guidance from a model for the internal wave energy source strength[9], was:

$$K(z) = \frac{K(z_r)}{[1 + \alpha(\sigma(z_r) - \sigma(z))]^2}$$

Here $\sigma(z)$ is the potential density, where $z_r = 500$ m, which is near the tops of the ridges in the vicinity of the release site and near the bottom of the tracer distribution, and $\alpha$ is a constant. Below $z_r$, where there is virtually no tracer at the end of the model period, $K$ was taken to be constant at its value at −500 m, for convenience. No-flux boundary conditions were enforced at $z = -800$ m and +500 m. The source or sink of water implicitly balancing $\partial w/\partial z$ carries no tracer, since the concentration is zero at the open side boundaries of the region modelled. The best fit was for $K(z_r) = 8\ \mathrm{cm^2\ s^{-1}}$ and $\alpha = 12\ \mathrm{m^3\ kg^{-1}}$, corresponding to $K(0) = 3\ \mathrm{cm^2\ s^{-1}}$.

### Dissipation data

Velocity microstructure data were acquired on the first two cruises with a free-fall instrument[12], deployed in 1997 in conjunction with the tracer sampling (Fig. 1a). From these, turbulent dissipation-rate estimates were derived following Polzin and Montgomery[13]. Adjustment for temporal and spatial biases occurred in three steps. First, temporal bias was addressed by assuming that turbulent dissipation was proportional to the flux of tidally generated internal-wave energy, which, in turn, is proportional to the mean-square tidal current[14]. Observed dissipation data ($\epsilon$) were scaled using $\bar{\epsilon}(z) = [\langle U^2\rangle/U^2(t)]\epsilon(z)$, where $\langle U^2\rangle$ is the mean-square barotropic current averaged over the period between tracer injection and sampling and $U(t)$ is the tidal current speed for the time of each dissipation estimate. A model[15] was used to estimate the tidal currents. Second, these scaled dissipation data were used to construct model profiles for three bathymetric classes: ridge crests, valleys, and the sloping regions between the two (Fig. 4). Each model profile is a function of local height above bottom. Third, spatial bias was treated by mapping dissipation at the target isopycnal onto a uniform grid with 25-km resolution spanning the area of the tracer patch. The depth of the target isopycnal was mapped using a second-order polynomial in latitude and longitude, fitted to density data in the interval 14–22° W, 19–25° S, and height above bottom was determined with a high-resolution bathymetric data set[16]. The appropriate bathymetric class of the dissipation model was used at each grid point and spatial weighting by the observed 1997 tracer concentration field at the target isopycnal was used to calculate the average dissipation. The diffusivity estimate was derived using the expression[17] $K = \Gamma\epsilon N^{-2}$ with the observed mean value of the buoyancy gradient ($N^2$) and a mixing efficiency ($\Gamma$) of 20%. Uncertainty in this estimate derives from stochastic variability in the dissipation and from an uncertainty of 100 m in the bathymetric data. An error analysis was carried out using Monte Carlo methods, and the resulting estimate of $K = 2.3 \pm 1\ \mathrm{cm^2\ s^{-1}}$ reflects the 68% confidence interval.

Received 25 June; accepted 22 November 1999.


1. Gregg, M. C. Scaling turbulent dissipation in the thermocline. *J. Geophys. Res.* **94,** 9689–9698 (1989).
2. Toole, J. M., Polzin, K. L. & Schmitt, R. W. Estimates of diapycnal mixing in the abyssal ocean. *Science* **264,** 1120–1123 (1994).
3. Polzin, K., Toole, J. & Schmitt, R. Finescale parameterizations of turbulent dissipation. *J. Phys. Oceanogr.* **25,** 306–328 (1995).
4. Hogg, N., Biscaye, P., Gardner, W. & Schmitz, W. J. Jr On transport and modification of Antarctic bottom water in the Vema Channel. *J. Mar. Res.* (Suppl.) **40,** 231–263 (1982).
5. Morris, M., Hogg, N. & Owens, W. B. Diapycnal mixing estimated from advective budgets in the deep Brazil Basin. *Int. WOCE Newslett.* **28,** 23–25 (1997).
6. Polzin, K. L., Toole, J. M., Ledwell, J. R. & Schmitt, R. W. Spatial variability of turbulent mixing in the abyssal ocean. *Science* **276,** 93–96 (1997).
7. Ledwell, J. R., Watson, A. J. & Law, C. S. Mixing of a tracer in the pycnocline. *J. Geophys. Res.* **103,** 21499–21529 (1998).
8. Bell, T. H. Lee waves in stratified flows with simple harmonic time dependence. *J. Fluid Mech.* **67,** 705–722 (1975).
9. Polzin, K. L. Inertial subrange solutions for the energy balance of the finescale internal wavefield. *J. Mar. Res.* (submitted).
10. Langseth, M. G. & Hobart, M. A. Interpretation of heat flow measurements in the Vema Fracture Zone. *Geophys. Res. Lett.* **3,** 241–244 (1976).
11. Ledwell, J. R. & Bratkovich, A. A tracer study of mixing in the Santa Cruz Basin. *J. Geophys. Res.* **100,** 20681–20704 (1995).
12. Schmitt, R. W., Toole, J. M., Koehler, R. L., Mellinger, E. C. & Doherty, K. W. The development of a fine- and microstructure profiler. *J. Atmos. Ocean. Tech.* **5,** 484–500 (1988).
13. Polzin, K. L. & Montgomery, E. T. in *Proc. Microstructure Sensors Workshop* (eds Agrawal, Y., Williams, A. & Goodman, L.) 109–115 (Sequoia Scientific Inc., Mercer Island, Washington 98040, USA, 1997).
14. Bell, T. H., Jr. Topographically generated internal waves in the open ocean. *J. Geophys. Res.* **80,** 320–327 (1975).
15. Egbert, G. D., Bennet, A. F. & Foreman, M. G. G. TOPEX/POSEIDON tides estimated using a global inverse model. *J. Geophys. Res.* **99,** 24821–24852 (1994).
16. Smith, W. H. F. & Sandwell, D. T. Bathymetric prediction from dense altimetry and sparse shipboard bathymetry. *J. Geophys. Res.* **99,** 21803–21824 (1994).
17. Osborn, T. R. Estimates of the local rate of vertical diffusion from dissipation measurements. *J. Phys. Oceanogr.* **10,** 83–89 (1980).



### Acknowledgements

Our research is funded by the US National Science Foundation. We thank our technical associates and the officers and crew of the RV *Seward Johnson* for their support.


Correspondence and requests for materials should be addressed to J.R.L. (e-mail: jledwell@whoi.edu).

# Osmotic generation of 'anomalous' fluid pressures in geological environments

**C. E. Neuzil**

*US Geological Survey, 431 National Center, Reston, Virginia 20192, USA*

**Osmotic pressures are generated by differences in chemical potential of a solution across a membrane. But whether osmosis can have a significant effect on the pressure of fluids in geological environments has been controversial, because the membrane properties of geological media are poorly understood[1]. 'Anomalous' pressures—large departures from hydrostatic pressure that are not explicable in terms of topographic or fluid-density effects—are widely found in geological settings, and are commonly considered to result from processes that alter the pore or fluid volume[2], which in turn implies crustal changes happening at a rate too slow to observe directly. Yet if osmosis can explain some anomalies, there is no need to invoke such dynamic geological processes in those cases. Here I report results of a nine-year *in situ* measurement of fluid pressures and solute concentrations in shale that are consistent with the generation of large (up to 20 MPa) osmotic-pressure anomalies which could persist for tens of millions of years. Osmotic pressures of this magnitude and duration can explain many of the pressure anomalies observed in geological settings. They require, however, small shale porosity and large contrasts in the amount of dissolved solids in the pore waters—criteria that may help to distinguish between osmotic and crustal-dynamic origins of anomalous pressures.**

The test was conducted in Cretaceous-age Pierre Shale in central South Dakota, USA. The shale at the site is saturated, has a permeability of $10^{-20}$ to $10^{-21}\ \mathrm{m^2}$, and is 70–80% clay, of which about 80% is mixed-layer smectite-illite[3,4]. The shale pore water contains ~3.5 g $\mathrm{l^{-1}}$ NaCl, with only minor amounts of other solutes. Four boreholes were drilled in the shale (Fig. 1), and the test was started by adding waters with different total dissolved solids (TDS) to the boreholes. Fluid squeezed from cores guided the test design, with one borehole receiving a near duplicate of the expelled fluid (designated borehole DUP), two receiving water with ten times the solute concentration (high-TDS boreholes HC1 and HC2), and one receiving deionized water (borehole DI) (see also Supplementary Information, section 1). For 9 years water levels were monitored with an electrical sounding cable, and samples of borehole waters were collected for analysis; the water level and TDS changes are plotted in Fig. 2.

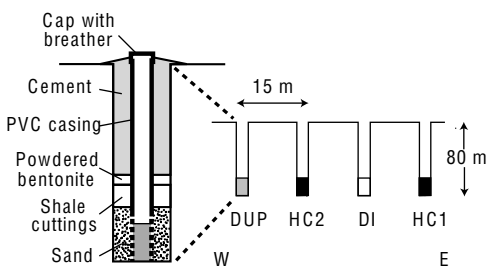


**Figure 1** Pierre Shale boreholes used for the osmosis test. The boreholes were capped to prevent rainfall or runoff from entering, but with breather holes to accommodate water level changes. Estimated evaporative losses from barometric pumping through the breather hole during the 9-year test were ~1 cm of water. The spacing between boreholes was chosen to ensure that they did not interact during the test.